




Article

Analysis of Metal-Insulator Crossover in Strained SrRuO₃ Thin Films by X-ray Photoelectron Spectroscopy

Andrea Nardi ^{1,2}, Chiara Bigi ^{1,2} , Sandeep Kumar Chaluvadi ¹ , Regina Ciancio ¹, Jun Fujii ¹, Ivana Vobornik ¹, Giancarlo Panaccione ¹, Giorgio Rossi ^{1,2}  and Pasquale Orgiani ^{1,3,*} 

¹ CNR-IOM, TASC Laboratory in Area Science Park, 34139 Trieste, Italy

² Department of Physics, University of Milano, 20133 Milano, Italy

³ CNR-SPIN, UOS Salerno, 84084 Fisciano (SA), Italy

* Correspondence: pasquale.orgiani@spin.cnr.it

Received: 13 July 2020; Accepted: 7 August 2020; Published: 11 August 2020



Abstract: The electronic properties of strontium ruthenate SrRuO₃ perovskite oxide thin films are modified by epitaxial strain, as determined by growing on different substrates by pulsed laser deposition. Temperature dependence of the transport properties indicates that tensile strain deformation of the SrRuO₃ unit cell reduces the metallicity of the material as well as its metal-insulator-transition (MIT) temperature. On the contrary, the shrinkage of the Ru–O–Ru buckling angle due to compressive strain is counterweighted by the increased overlap of the conduction Ru-4d orbitals with the O-2p ones due to the smaller interatomic distances resulting into an increased MIT temperature, i.e., a more conducting material. In particular, in the more metallic samples, the core level X-ray photoemission spectroscopy lineshapes show the occurrence of an extra-peak at the lower binding energies of the main Ru-3d peak that is attributed to screening, as observed in volume sensitive photoemission of the unstrained material.

Keywords: metal-insulator-transition; perovskite oxides; laser deposition; stress-strain relations; angular resolved photoemission spectroscopy; X-ray photoemission spectroscopy

1. Introduction

Electron hybridization in solids in competition with Coulomb interactions plays a fundamental role in the quantum properties of these transition metal oxide materials [1–7]. In the context of spintronics, magnetic and electronic reconstructions at the interface have been often reported, with their origin lying in the delicate interplay between the charge, spin and orbital degrees of freedom. Looking at the strength of electron hybridization and localization, near a surface or interface the reduced translational symmetry modifies the electronic properties with important consequences on the magnetic order parameter, the transition temperature and the metallic vs. insulating behaviour, thus hindering the achievement of the desired performance of interface-based devices.

Strontium ruthenate SrRuO₃ (SRO) is an itinerant ferromagnet and a prototypical spintronics system [8,9]. Because of the structural and chemical similarities of all oxide perovskites, the growth of very high-quality epitaxial SRO-based heterostructures is indeed possible, thus allowing to explore new perspectives in the field of electronic, magnetic and optical devices [10–12]. Yet, interest in SRO goes well beyond its use as a functional layer embedded in oxide heterostructures. As a matter of fact, several works have provided evidence of a strong correlation between transport, magnetic and structural properties of SRO making it a very interesting model material for the study of itinerant magnetism in oxide systems [8,13–18]. However, as in many other oxide materials, surface- (or more

in general interfacial-) and defect states play critical roles in mediating ferromagnetism, due to the modified chemistry of the first top—or interfacial—layers.

Here we report on the influence of the epitaxial strain on the electronic properties of SRO thin films at the surface. Epitaxial thin films were grown on different substrates by pulsed laser deposition (PLD) technique, characterized by crystallography and their properties were probed by electron spectroscopy. As expected, the metal-insulator-temperature T_{MI} turns out to be modulated by the in-plane biaxial strain (it increases in compressively strained films, while it decreases in tensile strained ones). Core level soft X-ray photoemission spectroscopy with tuneable synchrotron radiation reveals the occurrence of an extra peak at Ru-3d, which is the signature of bulk-like hybridization and metallicity, only in the most metallic SRO films. In particular, only compressively strained SRO thin films display bulk-like electronic properties also in proximity of the surface (i.e., within 1 nm) as opposite to SRO films under tensile strain. This evidence that the surface/interface electronic charge distribution can be effectively controlled via atomic-precision growth techniques, is of importance for possible applications in the field of integrated spintronics.

2. Materials and Methods

PLD growth of epitaxial SRO thin films was performed using a KrF excimer pulsed laser source, with a typical energy density per laser shot of about 3 J/cm^2 and a laser repetition rate of 3 Hz ablating from a SRO stoichiometric target (purity at 99.99%). The films growth was performed in an ultra-pure oxygen background atmosphere (purity at 99.9999%). All of the investigated samples were grown at 0.1 mbar with a substrate temperature at $500 \text{ }^\circ\text{C}$. After the film growth, the samples were cooled down to room temperature in about 15 min in oxygen at the same deposition pressure. Structural characterization was carried out using a four-circle Panalytical X'pert diffractometer with a Cu K_α radiation source. Surface morphology of the SRO samples was investigated by a Supra 40 field-emission gun (FEG) scanning electron microscope (SEM) equipped with a Gemini column and an In-lens detector yielding increased signal to noise ratio. EDS experiments were carried out by Oxford LN_2 -free X-Act Silicon Drift Detector and chemical composition were calculated by Aztec software. Soft X-ray radiation spectroscopy (XPS and ARPES) and LEED experiments were carried out at the APE-IOM beamlines at Elettra. The measurements were recorded on the samples that were transferred in situ directly after growth under UHV conditions (base pressure $< 2 \times 10^{-10}$ mbar) to the APE spectrometer end stations. XPS spectra were taken with a photon energy of 900 eV with an Omicron E125 hemispherical analyzer. The ARPES data were acquired with linearly polarized synchrotron radiation and a Scienta DA-30 hemispherical analyser.

3. Structural Properties

SRO possesses an orthorhombic crystal structure with lattice constants $a = 0.556 \text{ nm}$, $b = 0.553 \text{ nm}$ and $c = 0.784 \text{ nm}$. Yet, it shows a perovskite-like sub-unit cell with lattice constants $a = b = c = 0.393 \text{ nm}$ for bulk material [19,20]. For the sake of simplicity in this paper, the Miller indices of SRO will be referred to the perovskite cell. In order to induce different in-plane biaxial strain, SRO thin films were grown on (110) NdGaO_3 (NGO), (001) SrTiO_3 (STO) and (110) GdScO_3 (GSO) single crystal substrates. Considering the SRO bulk lattice parameter of 0.393 nm, SRO films are expected to grow strained under compressive (i.e., -1.8% and -0.6% on NGO and STO, respectively) or tensile (i.e., $+0.9\%$ on GSO) conditions. Deposition of SRO thin films was optimized at 0.1 mbar of ultra-pure oxygen pressure without any post-annealing process of the samples. Since the high-pressure background condition during the growth (i.e., 0.1 mbar) could possibly affect the stoichiometric ratio of the heavy-ion elements [21–23], energy dispersive spectroscopy (EDS) analysis was performed. Because of the overlap between the characteristic peaks of SRO film with some elements present in the substrates, a reliable stoichiometric analysis was obtained by performing the EDS analysis on SRO films grown on NGO substrates (Figure 1).

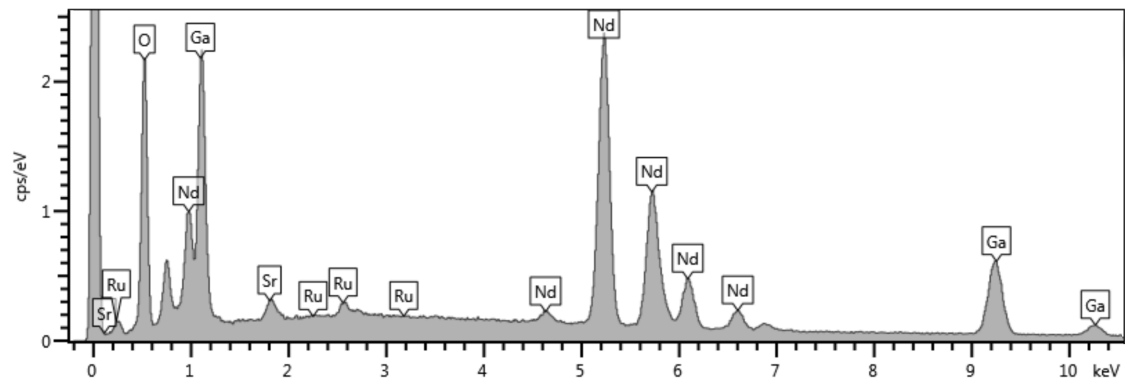


Figure 1. EDS spectrum of SRO film grown on NGO substrate.

EDS experiments confirm that SRO films grown at 0.1 mbar, with a target-to-substrate of 5 cm and by using high energy laser pulses of 300 mJ show the optimal heavy-ion stoichiometric ratio (namely, Sr:Ru = 1:1—with an experimental error of about 5%). X-ray diffraction (XRD) characterization was routinely performed for all of the samples. The θ - 2θ scans in symmetrical Bragg-Brentano configuration for optimized SRO films only contain (001) peaks, indicating the preferential c -axis orientation of the films (in left a) of Figure 2 data refers to a SRO sample grown on NGO substrate). As expected, the out-of-plane lattice parameters evolve as a consequence of the substrate-induced strain mechanism (data are reported in panel b) of Figure 2).

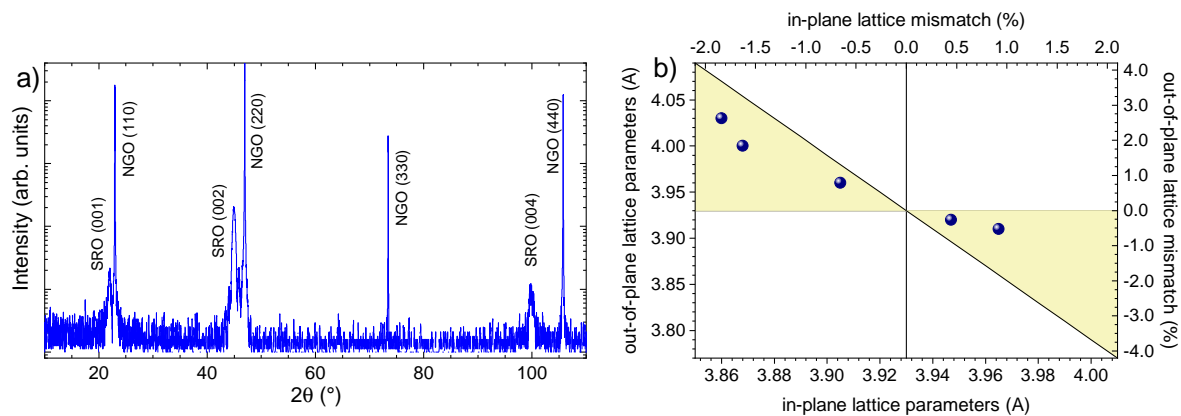


Figure 2. (a) symmetrical θ - 2θ scan of a SRO film grown on a (110)-oriented NGO substrate; (b) out-of-plane vs in-plane lattice parameters for the investigated SRO samples; the expected out-of-plane lattice deformation due to the elastic response of the lattice parameters as a function of a biaxial strain obtained by the Equation (1) is enlightened by the yellow area.

An in-plane compressive (tensile) strain induces the elongation (contraction) of the out-of-plane lattice parameters. In particular, the elastic response of the lattice parameters as a function of a biaxial strain can be obtained by the formula

$$\frac{\Delta c}{c} = -\frac{2\nu}{1-\nu} \cdot \frac{\Delta a}{a} \quad (1)$$

where ν is the Poisson ratio which can range between 0 and 0.5 (typical values found in oxides is 0.33). All of the measured structural deformations are compatible with elastic strain mechanism only (Figure 2b). The film thickness and surface roughness were probed by low-angle X-ray reflectivity (XRR). Representative XRR measurement of a SRO sample is shown in the Figure 3a.

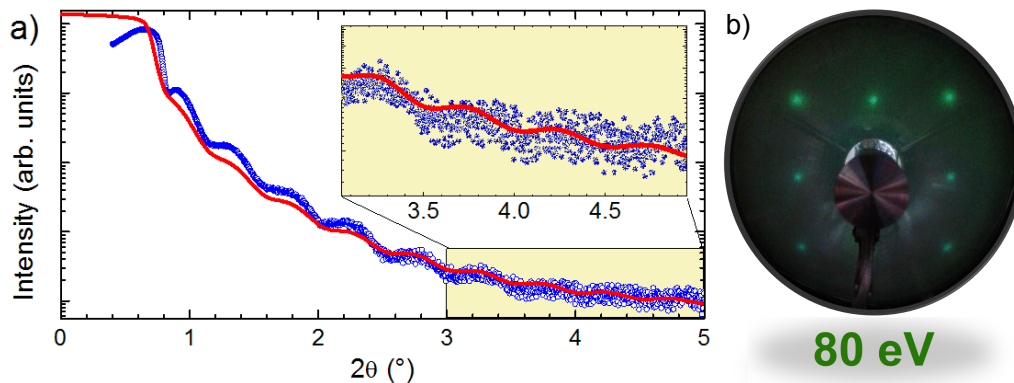


Figure 3. (a) low-angle X-ray reflectivity of a SRO film grown on a (110)-oriented NGO (blue circles along with the simulated curve (red)); (b) LEED patterns of a SRO film grown on a (110)-oriented NGO taken with electron energy of 80 eV.

Simulations of the low-angle XRR data were performed by mean of the IMD 4 package of XOP 2.3 software [24,25]. The fitted curves (red curves included in Figure 3a) nicely match the expected value of 15 nm. XRR oscillations are recorded up to 2θ values of 5° , while, above this angle, the oscillations fall below the experimental sensitivity of our X-ray diffractometer [26,27]. Surface long range order was probed by in situ low-energy electron diffraction (LEED). Figure 3b reports the LEED pattern of a SRO film grown on STO substrate, measured by electrons with 80 eV kinetic energy, which shows sharp diffraction spots arranged in an in-plane squared coordination of the pseudocubic SRO structure.

4. Transport Properties

Electrical transport measurements were carried out by standard four-probe dc technique, with a bias pulsed and reversed current. Here we report the resistivity versus temperature behaviour of SRO films grown on NGO (-1.8% compressive strained), STO (-0.6% compressive strained) and GSO ($+0.9\%$ tensile strained) substrates (Figure 4a).

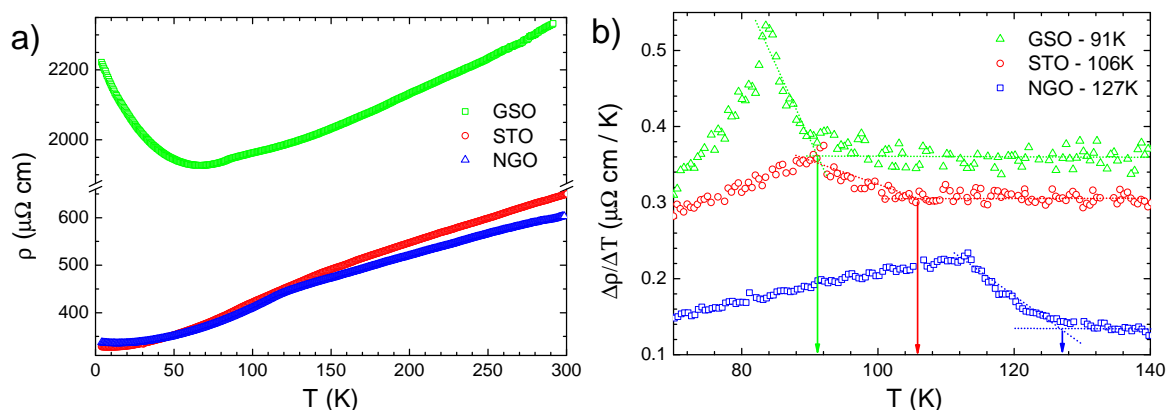


Figure 4. (a) Resistivity versus temperature curves for SRO films grown on NGO (blue triangles), STO (red circles) and GSO (green triangles); (b) Derivative of resistivity as a function of temperature for the three reported samples (i.e., color code is the same).

Among these, SRO film deposited on GSO substrates shows the highest resistivity values and a very small residual resistivity ratio (RRR) value (slightly larger than 1), indicating a higher degree of structural disorder in the film [28–30]. The negative slope of the resistivity curve in the low temperature range ($T < 50$ K) is consistent with the presence of impurities that act as scattering centres determining the insulating character of SRO film on GSO at low temperatures [31]. Conversely, SRO film grown on NGO substrate is the most metallic one, across the whole temperature range, with room temperature resistivity of about $600 \mu\Omega\cdot\text{cm}$, which is very close to those reported for SRO thin films [32] while

thicker films are characterized by lower (i.e., factor of 2) values [13,14,33]. Moreover, the RRR of SRO film grown on NGO is a few percent smaller than the STO sample, which can indicate that the STO substrate (i.e., low strain imposed) might favor better structural properties (i.e., less defects). The paramagnetic to ferromagnetic transition in SRO is associated to a change in the resistivity curve, namely from a linear- T to a parabolic- T^2 behaviour at high and low temperatures, respectively [8,34]. In this respect, the analysis of the derivative $\Delta\rho/\Delta T$ provides the evaluation of the T_{MI} temperature by the onset of its increase at low temperatures (see arrows in Figure 4b). The T_{MI} temperature is severely reduced in the case of the film grown on GSO (91 K) film with respect to the SRO samples grown on STO (i.e., 106 K) and NGO (i.e., 127 K).

5. ARPES Experiments

Photoemission investigation was performed with polarized synchrotron radiation on SRO films transferred in situ (base pressure during the transfer never exceeds 2×10^{-10} mbar) directly after the growth, to the two end-stations of the APE beamline [35]. Such a strategy allowed us to perform spectroscopic experiments on pristine uncontaminated samples [36–38]. In particular, the most metallic SRO film (i.e., the one grown on NGO substrate) was investigated by means of ARPES. Measurements were performed at room temperature. Figure 5 shows the ARPES energy dispersion map obtained with linearly polarized light of $h\nu = 70$ eV. Two arcs dispersing near ± 0.5 confirm.

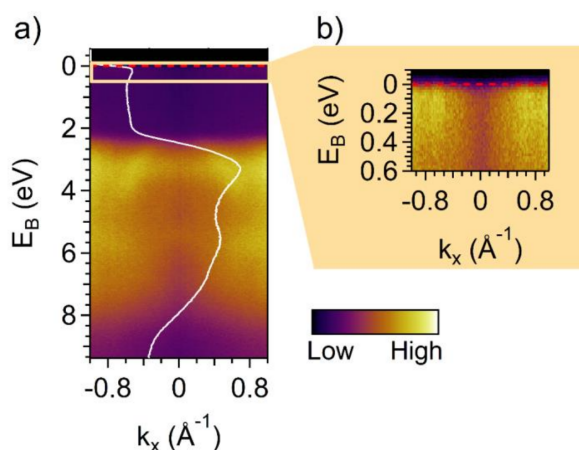


Figure 5. ARPES energy dispersion map of SrRuO₃ measured with 70 eV photon energy at room temperature. (a) Valence band dispersion and angle-integrated DOS showing spectral intensity at the Fermi level (white profile superimposed to ARPES spectrum). (b) Zoom to the area close to the Fermi level indicating the states responsible for the metallic nature of the film.

The integrated density of state (DOS) is superimposed to ARPES map of Figure 5 (white solid line). In particular, the spectral weight close to the Fermi level is ascribed to the Ru-4d t_{2g} orbital, while the valence band (VB) is mainly associated to O-2p orbitals [39]. The overall DOS shape is consistent with those reported in the literature, showing the VB bandwidth spans between 8 and 1.8 eV binding energy [39,40]. Some discrepancies in the ARPES data are ascribable to the different experimental conditions. In particular, a tiny electron pocket centred at $k_x = 0$ is missing in our spectra, while it is reported in refs [40,41] but not in ref [42]. However, at difference to our case, the data in other reports were mainly acquired using unpolarized He-I radiation (21.2 eV) at $T < 15$ K [40–42]. The observed discrepancies are therefore consistent either with a different Brillouin zone sampling due to the excitation energy either to matrix element effects induced by light polarization or experimental geometry. The overall good consistency between our data and those reported in literature [40–43] is indicative of optimal stoichiometry bulk-like electronic properties of SRO samples grown on NGO. In particular, due to the high surface sensitivity intrinsic to ARPES technique, such properties are maintained up to the very surface of the films (i.e., 3–4 Å).

6. Core Level Photoemission Spectroscopy Experiments

Soft X-ray photoemission spectroscopy (XPS) spectra were measured at room temperature with linearly polarized synchrotron radiation on SRO samples transferred in situ directly after growth. The near surface properties of the SRO thin films were quantitatively explored by measuring the relative intensities of core-level photoemission spectra as well as the valence density of states (Figure 6) [44–48].

The XPS survey scan displays the main peaks of both Sr and Ru with no trace of material segregation. Moreover, the XPS spectra of the valence band show differences in the density of states in the Fermi level region that reflect the transport results discussed above. The connection between strain and metallic character can be seen from the changes at the Fermi level: the density of states becomes larger for the compressively strained samples (i.e., NGO and STO) compared with the tensile strained one (GSO) thus confirming that SRO grown with the most compressive strain possesses has a clear metallic character up to the surface. XPS of the Ru-3d, Sr-3p and O1s peaks were investigated in the most metallic sample. Even though Sr-3p^{1/2} peak partially overlap Ru-3d^{3/2}, a doublet structure can be clearly seen at Ru-3d. These peaks were attributed to well-screened (lower binding energy peak) and poorly screened (unscreened—higher binding energy peak) components arising in the photoemission process [44,49–51]. Consistently, O-1s peak also shows a double-peaks structure, with the satellite peak attributed to an electron screening mechanism [52]. In order to correlate the presence of the Ru-3d extra-peak with the metallicity of the system, lineshapes of Ru-3d and Sr-3p peaks were analyzed in all SRO samples (Figure 7).

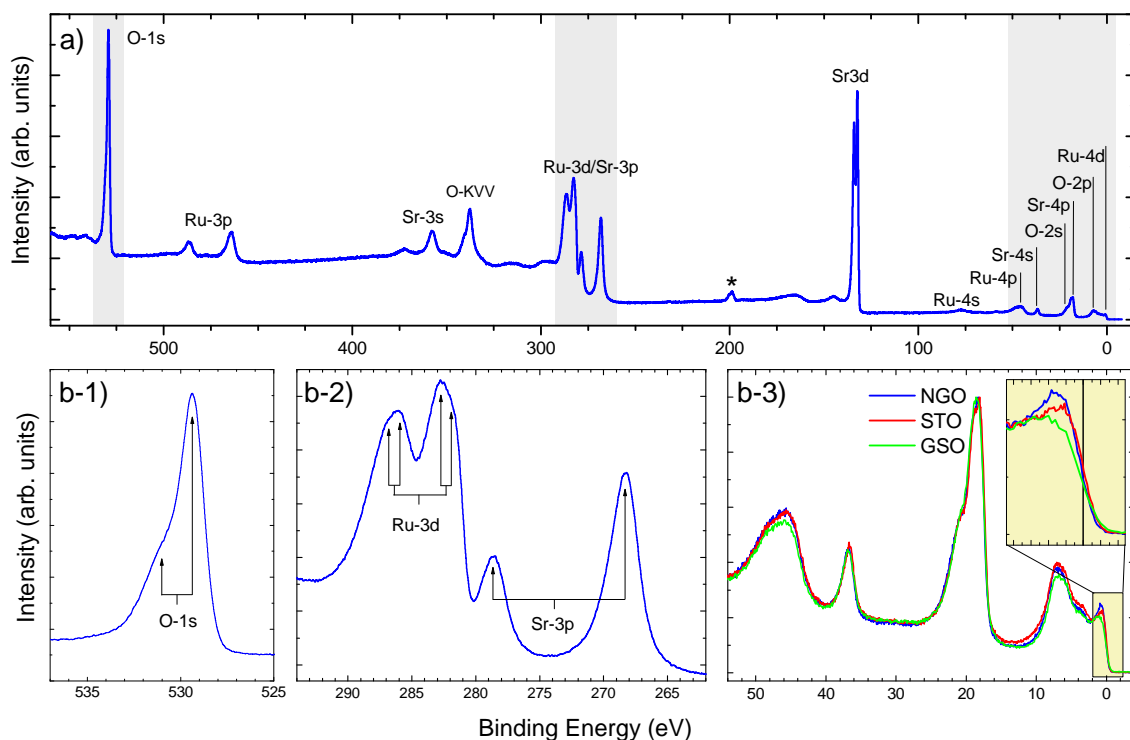


Figure 6. (a) XPS survey scan of a SRO film grown on NGO substrate (excitation photon energy was $h\nu = 850$ eV); (b) high-resolution XPS scans of O-1s (b-1) and Ru-3d/Sr-3p (b-2) core levels, along with the valence band (b-3); In particular, valence band scans are reported for all of investigated SRO samples (i.e., namely grown on NGO (blue), STO (red) and GSO (green), respectively; in the inset, a zooming out of the Fermi's edge).

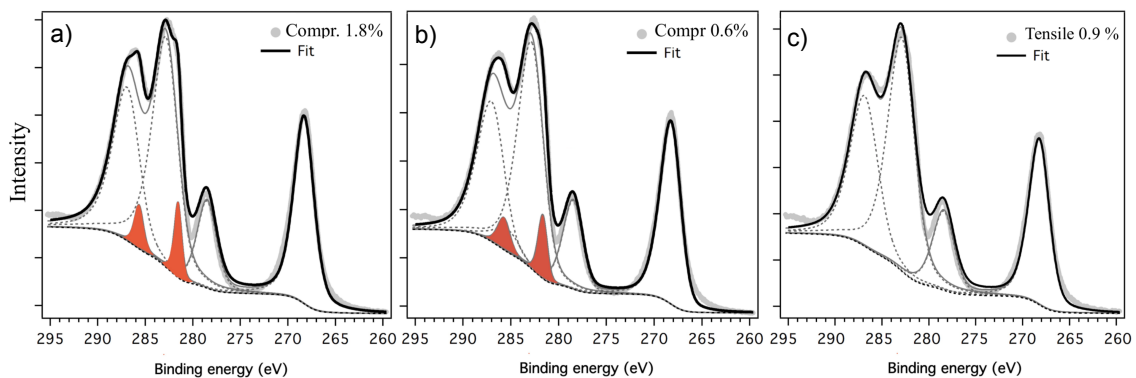


Figure 7. High-resolution XPS scans of Ru-3d/Sr-3p peaks for SRO films grown on NGO (a), STO (b) and GSO (c); photon energy was $h\nu = 850$ eV. Results of fitting procedures are also reported (area of well-screened peak in enlighten by red filling color).

The best fit was obtained allowing for two energy shifted components for Ruthenium, consistently with the reference papers [44,45,51]. The intensity ratios between the two components of each spin-orbit doublet are 4/3 for Ru-3d and 1/2 for Sr-3p. By comparing the Ru-3d spectra with those reported for nearly perfectly stoichiometric SRO [44–46]. Moreover, in tensile-strained SRO sample with low metallicity (i.e., SRO on GSO), the well-screened peak is suppressed while it is well-defined in compressive-strained highly metallic ones (i.e., SRO grown on NGO and STO).

7. Conclusions

The ensemble of photoelectron spectroscopy results shows how both the buckling of the bond angle and the changes in the bond length must both be considered to explain the electronic transport properties. The width of the conduction band strongly depends on the superimposition of the oxygen O-2p $_{\sigma}$ and O-2p $_{\pi}$ orbitals and Ru-4d orbitals. On one hand, tensile strain—occurring in SRO samples grown on GSO—tends to make the structure near-cubic (i.e., the Ru-O-Ru buckling angle decreases) thus better aligning Ru-4d and O-2p orbitals. On the other hand, the increased inter-atomic distance makes such a superimposition smaller thus resulting in a less conductive sample, as shown from the increase in resistivity. Differently, compressive strain—occurring in SRO samples grown on NGO and STO—increases the conductivity albeit it shrinks the Ru-O-Ru angle, meaning that the overlap of the conduction orbitals is increased by the smaller interatomic distance in spite of their axes becoming more misaligned. The very presence of the Ru-3d well-screened peak in the soft X-ray photoemission spectra demonstrates that compressively strained SRO thin films display bulk like electronic properties also in proximity of the surface.

Author Contributions: Conceptualization P.O.; methodology, A.N., C.B., S.K.C., R.C., J.F., I.V., G.P., G.R., and P.O.; software, A.N. and P.O.; validation, A.N., C.B., S.K.C., R.C., J.F., I.V., G.P., G.R., and P.O.; formal analysis, A.N., G.R., and P.O.; writing—original draft preparation, A.N., G.R., and P.O.; writing—review and editing, A.N., C.B., S.K.C., R.C., J.F., I.V., G.P., G.R., and P.O.; All authors have read and agreed to the published version of the manuscript.

Funding: This research received no external funding.

Acknowledgments: This work is performed in the framework of the Nanoscience Foundry and Fine Analysis (NFFA-MIUR Italy Progetti Internazionali) facility.

Conflicts of Interest: The authors declare no conflict of interest.

References

1. Van V.M. Competition between screening channels in core-level X-ray photoemission as a probe of changes in the ground-state properties of transition-metal compounds. *Phys. Rev. B Condens. Matter Mater. Phys.* **2006**, *74*, 085118.

2. Horiba, K.; Taguchi, M.; Chainani, A.; Takata, Y.; Ikenaga, E.; Miwa, D.; Nishino, Y.; Tamasaku, K.; Awaji, M.; Takeuchi, A.; et al. Nature of the well screened state in hard X-ray Mn 2p core-level photoemission measurements of $\text{La}_{1-x}\text{Sr}_x\text{MnO}_3$ films. *Phys. Rev. Lett.* **2004**, *93*, 236401. [[CrossRef](#)]
3. Offi, F.; Mannella, N.; Pardini, T.; Panaccione, G.; Fondacaro, A.; Torelli, P.; West, M.W.; Mitchell, J.F.; Fadley, C.S. Temperature-dependent electronic structure of the colossal magnetoresistive manganite $\text{La}_{0.7}\text{Sr}_{0.3}\text{MnO}_3$ from hard X-ray photoemission. *Phys. Rev. B Condens. Matter Mater. Phys.* **2008**, *77*, 174422. [[CrossRef](#)]
4. Panaccione, G.; Altarelli, M.; Fondacaro, A.; Georges, A.; Huotari, S.; Lacovig, P.; Lichtenstein, A.; Metcalf, P.; Monaco, G.; Offi, F.; et al. Coherent peaks and minimal probing depth in photoemission spectroscopy of mott-hubbard systems. *Phys. Rev. Lett.* **2006**, *97*, 116401. [[CrossRef](#)] [[PubMed](#)]
5. Sandell, A.; Jaworowski, A.J. The Mn 2p core-level photoelectron spectrum of Pd-Mn bimetallic systems on Pd(100). *J. Electron Spectrosc. Relat. Phenom.* **2004**, *135*, 7–14. [[CrossRef](#)]
6. Schlueter, C.; Orgiani, P.; Lee, T.L.; Petrov, A.Y.; Galdi, A.; Davidson, B.A.; Zegenhagen, J.; Aruta, C. Evidence of electronic band redistribution in $\text{La}_{0.65}\text{Sr}_{0.35}\text{MnO}_{3-\delta}$ by hard X-ray photoelectron spectroscopy. *Phys. Rev. B Condens. Matter Mater. Phys.* **2012**, *86*, 155102. [[CrossRef](#)]
7. Pincelli, T.; Lollobrigida, V.; Borgatti, F.; Regoutz, A.; Gobaut, B.; Schlueter, C.; Lee, T.L.; Payne, D.J.; Oura, M.; Tamasaku, K.; et al. Quantifying the critical thickness of electron hybridization in spintronics materials. *Nat. Commun.* **2017**, *8*, 16051. [[CrossRef](#)]
8. Koster, G.; Klein, L.; Siemons, W.; Rijnders, G.; Dodge, J.S.; Eom, C.B.; Blank, D.H.A.; Beasley, M.R. Structure, physical properties, and applications of SrRuO_3 thin films. *Rev. Mod. Phys.* **2012**, *84*, 253–298. [[CrossRef](#)]
9. Pang, S. Review on electronic correlations and the metal-insulator transition in SrRuO_3 . *Appl. Microsc.* **2017**, *47*, 187–202. [[CrossRef](#)]
10. Nair, H.P.; Liu, Y.; Ruf, J.P.; Schreiber, N.J.; Shang, S.-L.; Baek, D.J.; Goodge, B.H.; Kourkoutis, L.F.; Liu, Z.-K.; Shen, K.M.; et al. Synthesis science of SrRuO_3 and CaRuO_3 epitaxial films with high residual resistivity ratios. *APL Mater.* **2018**, *6*, 046101. [[CrossRef](#)]
11. Wang, Z.; Nair, H.P.; Correa, G.C.; Jeong, J.; Lee, K.; Kim, E.S.; Seidner, A.; Lee, C.S.; Lim, H.J.; Muller, D.A.; et al. Epitaxial integration and properties of SrRuO_3 on silicon. *APL Mater.* **2018**, *6*, 086101. [[CrossRef](#)]
12. Schraknepper, H.; Baumer, C.; Gunkel, F.; Dittmann, R.; De Souza, R.A. Pulsed laser deposition of SrRuO_3 thin-films: The role of the pulse repetition rate. *APL Mater.* **2016**, *4*, 126109. [[CrossRef](#)]
13. Klein, L.; Dodge, J.S.; Ahn, C.H.; Reiner, J.W.; Mieville, L.; Geballe, T.H.; Beasley, M.R.; Kapitulnik, A. Transport and magnetization in the badly metallic itinerant ferromagnet SrRuO_3 . *J. Phys. Condens. Matter* **1996**, *8*, 10111–10126. [[CrossRef](#)]
14. Chen, C.L.; Cao, Y.; Huang, Z.J.; Jiang, Q.D.; Zhang, Z.; Sun, Y.Y.; Kang, W.N.; Dezaneti, L.M.; Chu, W.K.; Chu, C.W. Epitaxial SrRuO_3 thin films on (001) SrTiO_3 . *Appl. Phys. Lett.* **1997**, *71*, 1047–1049. [[CrossRef](#)]
15. Jiang, J.C.; Tian, W.; Pan, X.Q.; Gan, Q.; Eom, C.B. Domain structure of epitaxial SrRuO_3 thin films on miscut (001) SrTiO_3 substrates. *Appl. Phys. Lett.* **1998**, *72*, 2963–2965. [[CrossRef](#)]
16. Gan, Q.; Rao, R.A.; Eom, C.B.; Garrett, J.L.; Lee, M. Direct measurement of strain effects on magnetic and electrical properties of epitaxial SrRuO_3 thin films. *Appl. Phys. Lett.* **1998**, *72*, 978–980. [[CrossRef](#)]
17. Orgiani, P.; Aruta, C.; Balestrino, G.; Lavanga, S.; Medaglia, P.G.; Tebano, A. Strain effect on transport properties of SrRuO_3 films grown by laser MBE. *Eur. Phys. J. B* **2002**, *26*, 23–28. [[CrossRef](#)]
18. Qin, Q.; Liu, L.; Lin, W.; Shu, X.; Xie, Q.; Lim, Z.; Li, C.; He, S.; Chow, G.M.; Chen, J. Emergence of topological hall effect in a SrRuO_3 single layer. *Adv. Mater.* **2019**, *31*, 1807008. [[CrossRef](#)]
19. Gausepohl, S.C.; Lee, M.; Char, K.; Rao, R.A.; Eom, C.B. Magnetoresistance properties of thin films of the metallic oxide ferromagnet SrRuO_3 . *Phys. Rev. B Condens. Matter Mater. Phys.* **1995**, *52*, 3459–3465. [[CrossRef](#)]
20. Bansal, C.; Kawanaka, H.; Takahashi, R.; Nishihara, Y. Metal-insulator transition in Fe-substituted SrRuO_3 bad metal system. *J. Alloy Compd.* **2003**, *360*, 47–53. [[CrossRef](#)]
21. Orgiani, P.; Ciancio, R.; Galdi, A.; Amoroso, S.; Maritato, L. Physical properties of $\text{La}_{0.7}\text{Ba}_{0.3}\text{MnO}_{3-\delta}$ complex oxide thin films grown by pulsed laser deposition technique. *Appl. Phys. Lett.* **2010**, *96*, 032501. [[CrossRef](#)]
22. Orgiani, P.; Bigi, C.; Kumar Das, P.; Fujii, J.; Ciancio, R.; Gobaut, B.; Galdi, A.; Sacco, C.; Maritato, L.; Torelli, P.; et al. Structural and electronic properties of Bi_2Se_3 topological insulator thin films grown by pulsed laser deposition. *Appl. Phys. Lett.* **2017**, *110*, 171601. [[CrossRef](#)]

23. Golalikhani, M.; Lei, Q.; Chandrasena, R.U.; Kasaei, L.; Park, H.; Bai, J.; Orgiani, P.; Ciston, J.; Sterbinsky, G.E.; Arena, D.A.; et al. Nature of the metal-insulator transition in few-unit-cell-thick LaNiO₃ films. *Nat. Commun.* **2018**, *9*, 2206. [[CrossRef](#)] [[PubMed](#)]
24. Windt, D.L. IMD—Software for modeling the optical properties of multilayer films. *Comput. Phys.* **1998**, *12*, 360. [[CrossRef](#)]
25. Sánchez del Río, M.; Dejus, R.J. XOP v2.4: Recent developments of the X-ray optics software toolkit. *Adv. Comput. Methods X-ray Opt. II* **2011**, *8141*, 814115.
26. Orgiani, P.; Perucchi, A.; Knez, D.; Ciancio, R.; Bigi, C.; Chaluvadi, S.K.; Fujii, J.; Vobornik, I.; Panaccione, G.; Rossi, G.; et al. Tuning the optical absorption of anatase thin films across the visible-to-near-infrared spectral region. *Phys. Rev. Appl.* **2020**, *13*, 044011. [[CrossRef](#)]
27. Bigi, C.; Orgiani, P.; Nardi, A.; Troglia, A.; Fujii, J.; Panaccione, G.; Vobornik, I.; Rossi, G. Robustness of topological states in Bi₂Se₃ thin film grown by Pulsed Laser Deposition on (001)-oriented SrTiO₃ perovskite. *Appl. Surf. Sci.* **2019**, *473*, 190–193. [[CrossRef](#)]
28. Kan, D.; Aso, R.; Kurata, H.; Shimakawa, Y. Epitaxial strain effect in tetragonal SrRuO₃ thin films. *J. Appl. Phys.* **2013**, *113*, 173912. [[CrossRef](#)]
29. Jeong, H.; Jeong, S.G.; Mohamed, A.Y.; Lee, M.; Noh, W.S.; Kim, Y.; Bae, J.S.; Choi, W.S.; Cho, D.Y. Thickness-dependent orbital hybridization in ultrathin SrRuO₃ epitaxial films. *Appl. Phys. Lett.* **2019**, *115*, 092906. [[CrossRef](#)]
30. Kim, D.; Lim, H.; Ha, S.S.; Seo, O.; Lee, S.S.; Kim, J.; Kim, K.J.; Perez Ramirez, L.; Gallet, J.J.; Bournel, F.; et al. Correlation between structural phase transition and surface chemical properties of thin film SrRuO₃/SrTiO₃ (001). *J. Chem. Phys.* **2020**, *152*, 034704. [[CrossRef](#)]
31. Chopdekar, R.V.; Takamura, Y.; Suzuki, Y. Disorder-induced carrier localization in ultrathin strained SrRuO₃ epitaxial films. *J. Appl. Phys.* **2006**, *99*, 08F503. [[CrossRef](#)]
32. Shen, X.; Qiu, X.; Su, D.; Zhou, S.; Li, A.; Wu, D. Thickness-dependent metal-insulator transition in epitaxial SrRuO₃ ultrathin films. *J. Appl. Phys.* **2015**, *117*, 015307. [[CrossRef](#)]
33. Maria, J.P.; Trolrier-McKinstry, S.; Schlom, D.G.; Hawley, M.E.; Brown, G.W. The influence of energetic bombardment on the structure and properties of epitaxial SrRuO₃ thin films grown by pulsed laser deposition. *J. Appl. Phys.* **1998**, *83*, 4373–4379. [[CrossRef](#)]
34. Capogna, L.; Mackenzie, A.P.; Mackenzie, A.P.; Perry, R.S.; Grigera, S.A.; Galvin, L.M.; Raychaudhuri, P.; Schofield, A.J.; Alexander, C.S.; Cao, G.; et al. Sensitivity to disorder of the metallic state in the ruthenates. *Phys. Rev. Lett.* **2002**, *88*, 766021–766024. [[CrossRef](#)] [[PubMed](#)]
35. Panaccione, G.; Vobornik, I.; Fujii, J.; Krizmancic, D.; Annese, E.; Giovanelli, L.; Maccherozzi, F.; Salvador, F.; De Luisa, A.; Benedetti, D.; et al. Advanced photoelectric effect experiment beamline at Elettra: A surface science laboratory coupled with Synchrotron Radiation. *Rev. Sci. Instrum.* **2009**, *80*, 043105. [[CrossRef](#)] [[PubMed](#)]
36. Gobaut, B.; Orgiani, P.; Sambri, A.; Di Gennaro, E.; Aruta, C.; Borgatti, F.; Lollobrigida, V.; Céolin, D.; Rueff, J.P.; Ciancio, R.; et al. Role of oxygen deposition pressure in the formation of Ti defect states in TiO₂ (001) anatase thin films. *ACS Appl. Mater. Interfaces* **2017**, *9*, 23099–23106. [[CrossRef](#)]
37. Bigi, C.; Orgiani, P.; Sławińska, J.; Fujii, J.; Irvine, J.T.; Picozzi, S.; Panaccione, G.; Vobornik, I.; Rossi, G.; Payne, D.; et al. Direct insight into the band structure of SrNbO₃. *Phys. Rev. Mater.* **2020**, *4*, 025006. [[CrossRef](#)]
38. Bigi, C.; Tang, Z.; Pierantozzi, G.M.; Orgiani, P.; Das, P.K.; Fujii, J.; Vobornik, I.; Pincelli, T.; Troglia, A.; Lee, T.L.; et al. Distinct behavior of localized and delocalized carriers in anatase TiO₂ (001) during reaction with O₂. *Phys. Rev. Mater.* **2020**, *4*, 025801. [[CrossRef](#)]
39. Fujioka, K.; Okamoto, J.; Mizokawa, T.; Fujimori, A.; Hase, I.; Abbate, M.; Lin, H.J.; Chen, C.T.; Takeda, Y.; Takano, M. Electronic structure of SrRuO₃. *Phys. Rev. B* **1997**, *56*, 6380. [[CrossRef](#)]
40. Yang, H.F.; Fan, C.C.; Liu, Z.T.; Yao, Q.; Li, M.Y.; Liu, J.S.; Jiang, M.H.; Shen, D.W. Comparative angle-resolved photoemission spectroscopy study of CaRuO₃ and SrRuO₃ thin films: Pronounced spectral weight transfer and possible precursor of lower Hubbard band. *Phys. Rev. B* **2016**, *94*, 115151. [[CrossRef](#)]
41. Shai, D.E.; Adamo, C.; Shen, D.W.; Brooks, C.M.; Harter, J.W.; Monkman, E.J.; Burganov, B.; Schlom, D.G.; Shen, K.M. Quasiparticle mass enhancement and temperature dependence of the electronic structure of ferromagnetic SrRuO₃ thin films. *Phys. Rev. Lett.* **2013**, *110*, 087004. [[CrossRef](#)] [[PubMed](#)]

42. Ryu, H.; Ishida, Y.; Kim, B.; Kim, J.R.; Kim, W.J.; Kohama, Y.; Imajo, S.; Yang, Z.; Kyung, W.; Hahn, S.; et al. Electronic band structure of (111) $SrRuO_3$ thin film—An angle-resolved photoemission spectroscopy study. *arXiv* **2020**, arXiv:2002.04256.
43. Yang, H.F.; Liu, Z.T.; Fan, C.C.; Yao, Q.; Xiang, P.; Zhang, K.L.; Li, M.Y.; Li, H.; Liu, J.S.; Shen, D.W.; et al. Origin of the kink in the band dispersion of the ferromagnetic perovskite $SrRuO_3$: Electron-phonon coupling. *Phys. Rev. B* **2016**, *93*, 121102. [[CrossRef](#)]
44. Kim, H.D.; Noh, H.J.; Kim, K.H.; Oh, S.J. Core-level X-ray photoemission satellites in ruthenates: A new mechanism revealing the Mott transition. *Phys. Rev. Lett.* **2004**, *93*, 126404. [[CrossRef](#)]
45. Kim, J.; Chung, J.; Oh, S.J. In situ photoemission study on $SrRuO_3/SrTiO_3$ films grown by pulsed laser deposition. *Phys. Rev. B Condens. Matter Mater. Phys.* **2005**, *71*, 121406. [[CrossRef](#)]
46. Siemons, W.; Koster, G.; Vailionis, A.; Yamamoto, H.; Blank, D.H.A.; Beasley, M.R. Dependence of the electronic structure of $SrRuO_3$ and its degree of correlation on cation off-stoichiometry. *Phys. Rev. B Condens. Matter Mater. Phys.* **2007**, *76*, 075126. [[CrossRef](#)]
47. Barlaz, D.E.; Haasch, R.T.; Seebauer, E.G. Epitaxial $SrRuO_3/SrTiO_3$ (100) analyzed using X-ray photoelectron spectroscopy. *Surf. Sci. Spectra* **2017**, *24*, 024002. [[CrossRef](#)]
48. Galal, A.; Hassan, H.K.; Atta, N.F.; Abdel-Mageed, A.M.; Jacob, T. Synthesis, structural and morphological characterizations of nano-Ru-based perovskites/RGO composites. *Sci. Rep.* **2019**, *9*, 7948. [[CrossRef](#)]
49. Takizawa, M.; Toyota, D.; Wadati, H.; Chikamatsu, A.; Kumigashira, H.; Fujimori, A.; Oshima, M.; Fang, Z.; Lippmaa, M.; Kawasaki, M.; et al. Manifestation of correlation effects in the photoemission spectra of $Ca_{1-x}Sr_xRuO_3$. *Phys. Rev. B Condens. Matter Mater. Phys.* **2005**, *72*, 060404. [[CrossRef](#)]
50. Panaccione, G.; Manju, U.; Offi, F.; Annese, E.; Vobornik, I.; Torelli, P.; Zhu, Z.H.; Hossain, M.A.; Simonelli, L.; Fondacaro, A.; et al. Depth dependence of itinerant character in Mn-substituted $Sr_3Ru_2O_7$. *New J. Phys.* **2011**, *13*, 053059. [[CrossRef](#)]
51. Cox, P.A.; Egdell, R.G.; Goodenough, J.B.; Hamnett, A.; Naish, C.C. The metal-to-semiconductor transition in ternary ruthenium (IV) oxides: A study by electron spectroscopy. *J. Phys. C Solid State Phys.* **1983**, *16*, 6221–6239. [[CrossRef](#)]
52. Morgan, D.J. Resolving ruthenium: XPS studies of common ruthenium materials. *Surf. Interface Anal.* **2015**, *47*, 1072–1079. [[CrossRef](#)]



© 2020 by the authors. Licensee MDPI, Basel, Switzerland. This article is an open access article distributed under the terms and conditions of the Creative Commons Attribution (CC BY) license (<http://creativecommons.org/licenses/by/4.0/>).